DOI: 10.21062/mft.2025.065 http://www.journalmt.com

The Influence of Solidification Route on As-cast Microstructures of Al-Cu-Li-Mg-Zr-Sc Alloy

Rostislav Králík (0000-0002-4436-9980), Lucia Bajtošová (0000-0002-4746-9231), Barbora Kihoulou (0000-0001-7960-9748), Tomáš Krajňák (0000-0002-1899-4483), Miroslav Cieslar (0000-0002-2801-3810)
Charles University, Faculty of Mathematics and Physics, Ke Karlovu 5, Prague, 121 16, Czechia
rostislav.kralik@thermofisher.com (current address), 96473937@o365.cuni.cz, barbora.krivska@matfyz.cuni.cz, tomas.krajnak@matfyz.cuni.cz, miroslav.cieslar@matfyz.cuni.cz

The influence of the casting method on the microstructures of Al-Cu-Li-Mg-Zr-Sc was examined. The techniques include mold casting, twin-roll casting, and melt spinning. Estimated solidification rates of up to 10^7 K·s^{-1} produce dendritic solidification with eutectic cells ranging from 500 nm to 50 μm, decorated by primary phase particles with thicknesses from 200 nm to 3 μm. Exceeding this solidification rate results in near-diffusionless solidification, which traps more solutes in the matrix. This type of solidification yields a more supersaturated material, with nearly 90% of the total Cu content in the matrix and a fine dispersion of nanoscale spherical precipitates, each with a diameter of less than 100 nm. The small addition of Sc during casting primarily affects the material at low cooling rates, where primary Sc-containing particles modify the grain boundary shape.

Keywords: Al-Cu-Li-Mg-Zr-Sc, Mold casting, Twin-roll casting, Melt-spinning, Diffusionless solidification

1 Introduction

Al-Cu-based alloys have been used as structural materials for over a century, primarily in the aerospace industry, due to their low density and relatively high strength resulting from the addition of Li [1]. The current generation of these alloys typically consists of Al-Cu-Li-Mg-Zr, such as the AA2195 alloy [1-5]. During artificial aging, Cu, Li, and Mg create various nanoscale strengthening precipitates, primarily the Al_2CuLi (T1) and Al_2Cu (θ') phases. Additionally, Mg reduces stacking fault energy when present as a solute in the matrix, which enhances the uniformity of the T1 precipitates and facilitates the formation of a minor strengthening phase, Al_2CuMg (S') [6]. Zr significantly refines the grain structure after appropriate thermomechanical treatment, although other transition metals, such as Sc, could further enhance this refinement [3]. However, nanoscale Al_3Sc and composite $Al_3(Sc,Zr)$ precipitates may coarsen beyond their coherency limit during extended heat treatment of standard ingot-cast alloys, losing critical beneficial properties [7]. Therefore, producing materials with finer cast structures is essential, as shorter high-temperature exposure after casting can promote the formation of Sc- and Zr-containing precipitates without significant coarsening.

The final distribution and density of strengthening phases in peak-aged materials depend on the initial cast structure, which is characterized by microstructural features—primary phase particle size, their distribution, and volume fraction, solid solution supersaturation, dendrite arm spacing, and eutectic cell size—all of which are affected by the solidification rate and the solidification profile associated with different casting methods. Three casting methods were selected to produce materials that enable the study of this influence across various solidification rates: ingot casting into a mold, twin-roll casting (TRC), and melt-spinning.

Conventional Al-Cu-Li-based alloys are cast using direct-chill (DC) or ingot processes and then shaped into the desired form. Both methods yield materials with solidification rates ranging from 0.1 to 10 K·s^{-1}, which are inhomogeneous on a macroscopic level [8]. The initial structures are typically coarse, featuring large eutectic cells, and require extended high-temperature heat treatments lasting over 10 hours [2,3]. The constituent phases in AA2195 and similar Al-Cu-Li-Mg systems often include the θ (Al_2Cu) phase, the Al_7Cu_2Fe phase when iron is present as an impurity, the S (Al_2CuMg) phase, and potential Al-Cu-Li-based T phases [1-3]. These phases are approximately five micrometers in size and are found along the boundaries of dendritic cells and grains that are over 100 micrometers in diameter [9-11].

TRC produces strips of material that are several millimeters thick. The solidification rate during TRC is higher than in conventional casting methods (≈1000 K·s^{-1}) and usually results in finer microstructures [12,13]. Slámová et al. [13] confirmed that TRC can reduce the grain size by 25% in materials made of the same alloy. Early work on TRC Al-Cu-Li-based alloys

[14] shows that primary phase sizes below one micrometer are much smaller compared to DC-cast alloys [3]. Studies using diffusion-based calculations confirm that refining eutectic cells in TRC Al-Cu-Li-Mg-Zr-Sc alloys can reduce the required homogenization time from several hours to less than one hour [15].

Melt-spinning is a rapid solidification (RS) method that produces thin strips of material by melting small amounts and spraying them through a narrow nozzle onto rapidly spinning, water-cooled rolls. These rolls are made of materials with high thermal conductivity, enabling them to achieve high solidification rates exceeding 10^6 K·s^{-1}. Such high cooling rates can prevent standard dendritic solidification and, under certain conditions, inhibit nucleation and grain growth, leading to the formation of glassy or amorphous structures [16]. Limited research exists on the melt-spinning of Al-Cu-Li-based alloys [17,18]. Kim and Cantor [18] report the refinement of eutectic cells to below three micrometers and the primary phase sizes along boundaries to less than one hundred nanometers. Other techniques, including spray forming, powder bed fusion, and isostatic pressing [19-21], have been employed to produce rapidly solidified Al-Cu-Li-based materials with varying degrees of success. Qi et al. [19] conducted spray-forming experiments, achieving an estimated cooling rate of 10^6 K·s^{-1}, comparable to melt-spinning. They observed a primary phase size of approximately one hundred nanometers, with these phases forming along dendritic cells. Gianogolio et al. [22] produced atomized binary Al-Cu particles at cooling rates up to 10^5 K·s^{-1}. An increasing supersaturation of Cu in the matrix was measured with higher cooling rates in the atomized particles. Additionally, a decrease in dendritic spacing and particle sizes as small as 500 nm was observed within the studied solidification rate range.

An often-overlooked effect of rapid solidification is constitutional supercooling and diffusionless solidification, which arises from the fast motion of the solidification interface, which exceeds the diffusivity of alloying elements. A complex study by Yang et al. [23] combined a phase field model with finite interface dissipation, and the results of experimental measurements show that with increased interface velocity, the gap between the solidus and liquidus curves of the phase diagram shrinks. This effect explains the interface velocity-dependent coefficient of solute segregation and high solute concentrations, which cannot be explained from equilibrium diagrams. According to Gusakova et al. [24,25], RS methods can reach thermal transfer coefficients as high as 10^7 W·K^{-1}·m^{-2}, which is significantly higher than in TRC materials (10^4 W·K^{-1}·m^{-2}) or conventional ingot castings (10^2 W·K^{-1}·m^{-2}) [24,26]. The high thermal transfer results in significant undercooling, which enables the solidification front to move at solidification speeds (v) higher than a critical value (v_{crit}). Gusakova et al. [24,25] categorize solidification into three distinct regimes, each producing identifiable zones at and around these critical solidification rates. Solidification at a speed higher than the critical speed forms a featureless region, which effectively traps all solutes, as they cannot diffuse to the solidification interface and remain frozen in place (Zone 1). The surplus solutes can then precipitate during cooling or at room temperature after the casting process. Thermal transfer through this solidified region is less efficient than thermal transfer directly into the cooled substrate, and the degree of undercooling and solidification velocity decreases. Cellular crystallization occurs once $v \approx v_{crit}$ (Zone 2). Solidification in this region is called almost partitionless, and the increased non-planar solidification interface traps impurities. It implies the regular formation of primary phases at the boundaries of the cellular regions, coupled with further precipitation similar to the featureless region inside the cellular grains during the decomposition of the rapidly solidified matrix. Regular dendritic growth occurs at sufficiently low thermal transfer coefficients and solidification speeds (Zone 3).

A direct relationship can be established between the cast microstructure and the solidification rate in the case of dendritic solidification. A theoretical equation for the relationship between secondary dendrite arm spacing (SDAS) and parameters of solidification – thermal gradient at the solid/liquid interface, G, and velocity of the dendrite tip, R, is as follows:

$$SDAS = A \cdot (G \cdot R)^{-n}, \quad (1)$$

Where:

n and A …Material-dependent constants (generally between 0.3 and 0.5 for Al alloys) [27,28].

However, Eskin et al. [27] point out the difficulty of determining the exact order of observed dendritic branches or the exact thermal gradient or dendrite tip velocity. Therefore, an alternative relationship validated by Flemings et al. [29] is commonly applied:

$$DAS\ [\mu m] = A \cdot V^{-n}, \quad (2)$$

Dendrite tip velocity and thermal gradient are substituted by solidification rate V, and SDAS is substituted by any observed dendrite arm spacing (DAS). Haadzadeh and Wells [30] state that this simplified model is only valid for solidification rates up to 10^6 K·s^{-1}. Higher solidification rates would be associated with diffusionless solidification, which does not produce dendrites, making modeling through DAS meaningless.

An equation almost identical to Equation (2), but with different constants, can be used for a similar plot of grain size (GS) variance with solidification rate as:

$$GS\ [mm] = B \cdot V^{-m}, \quad (3)$$

Where:

B and m…Equivalents of A and n from Equation (2) [27,28].

The primary aim of this study is to estimate the solidification rate from the as-cast structures of Al-Cu-Li-Mg-Zr-(Sc) alloys. To accomplish this, three casting methods—mold casting, TRC, and melt spinning—with significantly different solidification rates were used to cast the materials under study. Investigating these three materials helps establish a relationship between the solidification rate of each method and key microstructural parameters—grain size, volume fraction of primary phases, primary phase size, and solid solution supersaturation—all of which influence the selection of optimal thermomechanical processing routes. Additionally, the twin-roll cast and mold-cast materials serve as references for identifying sharp behavioral changes associated with diffusionless solidification in the rapidly solidified melt-spun strips. Materials formed under diffusionless solidification conditions can exhibit vastly improved as-cast structures, particularly in terms of solute distribution homogeneity and primary phase refinement. A version of the alloy without Sc was used as a reference. Although Sc is mainly added to influence recrystallization during downstream processing, its effect on the as-cast states of this alloy class was also examined.

2 Materials and experimental methods

The composition of the alloys studied is listed in Table 1. The text also references two alloys: alloy A (AlCuLiMgZrSc) and alloy B (AlCuLiMgZr). The composition was determined using multiple optical emission spectroscopy measurements with the Bruker Q4 TASMAN spectroscope on both mold-cast and twin-roll cast materials. The input material for melt-spinning was obtained by remelting as-cast pieces of TRC strips. Cu and Li are the primary strengthening elements. Zr and Sc in alloy A act as grain refiners. Fe is present as an impurity. Mg can form strengthening precipitates but is mainly added to reduce stacking fault energy and enhance precipitation of the Al_2CuLi (T1) phase during aging. Ag performs a similar role as Mg.

Tab. 1 *Composition of the studied materials in wt. %. Experimental scatter in brackets to the last significant digit*

Element	Cu	Li	Mg	Zr	Sc	Ag	Fe	Al
Alloy A	2.60(8)	0.71(8)	0.27(2)	0.12(6)	0.16(4)	0.24(7)	0.10(6)	bal.
Alloy B	2.51(9)	0.73(6)	0.28(2)	0.11(7)	-	0.24(8)	0.09(6)	bal.

The mold-cast materials (MC) were melted at 900 °C in an argon atmosphere and cast into an air-cooled graphite mold. This original ingot measured 110 x 56 x 26 mm^3. The surface of the ingots was scalped after casting. The dimensions of the provided ingots are 85 x 50 x 22 mm^3.

The twin-roll cast (TRC) materials were produced using a vertical caster with steel outer shells. The strips measured approximately 3 mm in thickness and 200 mm in width. The alloys were melted under a protective argon atmosphere at 900 °C. The pouring temperature of the alloys was 660 °C. The casting speed for both alloys was set at 3.6 $m \cdot s^{-1}$. The total length of the strips ranged from 2 m to 3 m. More details about this casting process can be found in a publication by Grydin et al. [31].

The melt-spun (MS) materials were cast using boron nitride nozzles positioned 0.22 mm from the copper roll, which has a diameter of 235 mm and spins at 1500 rpm. The combination of roll size and rotation speed yields a linear speed of 37 $m \cdot s^{-1}$. Both materials were preheated to 1000 °C before casting. Alloy A was cast through a 10 x 0.55 mm^2 nozzle, while alloy B used a 6 x 0.8 mm^2 nozzle. A wider nozzle was used for alloy A to produce a more coherent strip, which was not achieved with the narrower nozzle.

The text describes the individual alloy and casting method combinations as MCA and MCB for the mold-cast alloys A and B, TRCA and TRCB for the twin-roll cast alloys A and B, and MSA and MSB for melt-spun alloys A and B.

Scanning electron microscopy (SEM) and scanning transmission electron microscopy (STEM) were used to analyze the cast materials. SEM studies were conducted with a Zeiss Auriga Compact and a Thermo Fisher Apreo 2 to examine the materials at mesoscopic and microscopic scales. Both backscattered electron (BSE) and secondary electron (SE) imaging modes were employed. The Zeiss microscope features a high-speed EDAX Velocity electron backscatter diffraction (EBSD) camera. Both microscopes are equipped with EDAX energy dispersive X-ray spectroscopy (EDS) detectors for element composition mapping. SEM samples were prepared using mechanical polishing with SiC papers and Struers OPS suspension of colloidal silica. Samples for EBSD were additionally electrochemically etched in a 33% HNO_3 in methanol solution at -15 °C for 3 seconds, using the Struers Lectropol 5 polisher. EBSD mapping and EDS measurements were carried out at a working distance of 12 mm, an accelerating voltage of 20 kV, and a 120 μm aperture. For higher-resolution imaging of the melt-spun materials, a (S)TEM JEOL 2200 FS was used, operating at 200 kV. Lamellar samples for STEM were prepared by Ga-focused ion beam (FIB) milling in the Zeiss Auriga Compact. The STEM system includes a JEOL Centurio EDS detector for mapping elemental distribution.

The mold-cast materials have no principal directions from which to evaluate them (Figure 1).

Longitudinal sections of TRC materials are investigated in SEM, and transversal sections of melt-spun materials are investigated in SEM and (S)TEM.

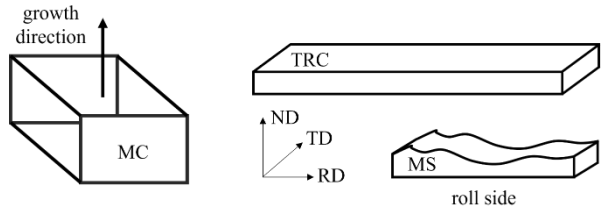

Fig. 1 *Schematic of the studied materials in the as-cast state and the principal/growth directions in relation to the materials*

3 Results

3.1 Mold casting

Figure 2 presents an example of grain orientation maps for a randomly selected 3 x 3 mm² area of the mold-cast materials. Orientations of grains are color-coded according to the standard inverse pole figure (IPF) triangle included in Figure 2. Both mold-cast materials have large grains with no subgrains. The grain size was measured using the circular intercept method based on the grain orientation maps (Figure 2) [32]:

$$\mathrm{GS} = 1.6\frac{l}{N_i}, \tag{4}$$

Where:

l…The circumference of the circle,

N_i…The number of intercepted grains. An average grain size is calculated from 10 measurements.

The average grain size of these materials is (156 ± 11) μm for the MCB and (130 ± 17) μm for the MCA materials (Figure 2). The grains in the MCB material are equiaxed, whereas the grain boundaries in the MCA material are irregular. This difference in grain shape is caused by clusters of primary phases containing Sc, which create strong retarding forces on the grain boundaries during casting. The Sc-rich clusters (highlighted by white arrows in the inset of Figure 2(b)) are observed at grain boundaries, pinning the boundaries in regions with irregular grain shapes.

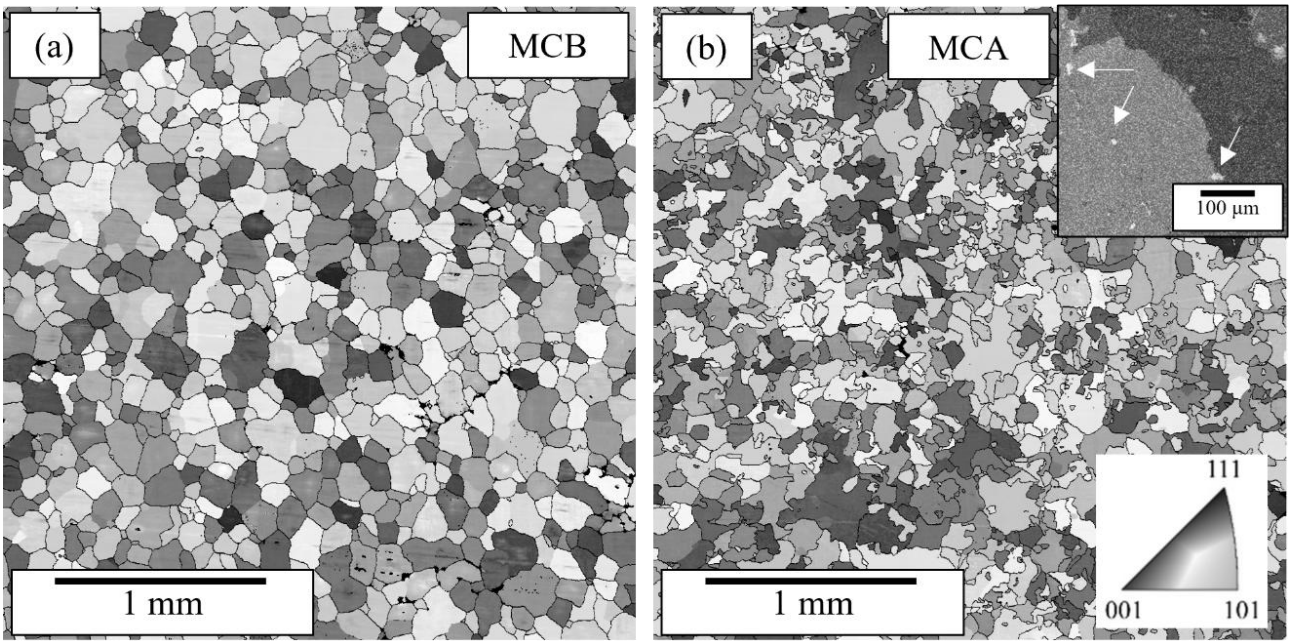

Fig. 2 *Grain orientation maps of 3x3 mm² sections of the mold-cast materials; (a) MCB material, (b) MCA material with an overlay of the Sc EDS map and the orientation map in the inset showing the pinning effect of the Sc-rich (white arrows) phase clusters; IPF triangle showing orientation color coding in the inset of (b)*

The constituent phases formed during the casting of this type of alloy, as observed by other researchers, are most often the θ(Al_2Cu) phase, the Al_7Cu_2Fe phase, or the S(Al_2CuMg) phase, along with the W($Al_{8-x}Cu_{4+x}Sc$ for x between 0 and 2.15) phase in the MCA material [1-3,33]. The presence of these phases is also confirmed by EDS mapping, showing that the constituents contain higher concentrations of Cu and are further locally enriched with Fe, Mg, or Sc in the MCSc material (Table 2). Li cannot be detected by EDS (Figure 3), but Li-containing precipitates (Al_6CuLi_3) have also been previously identified in these kinds of materials [34]. The formation of the W($Al_{8-x}Cu_{4+x}Sc$) phase is a harmful effect caused by slow solidification and cooling rates. However, DePottey et al. [33] observe the segregation of Sc to the eutectic Al-Cu θ-phase during casting and the formation of the W phase at cooling rates between 0.1 $K \cdot s^{-1}$ and 1 $K \cdot s^{-1}$, with a lack of this phase at cooling rates above 10 $K \cdot s^{-1}$.

The eutectic cell boundary phases are rod-shaped in the observation plane and measure (34 ± 10) μm in

length and (3.0 ± 1.5) μm in width (Figure 4). The averages are calculated from measurements of ten particles. The W($Al_{8-x}Cu_{4+x}Sc$) phase appears as an irregular cluster of particles. The size of these clusters is (11 ± 5) μm (Figure 3 (p,v)). The concentration of primary solutes and impurities in the intragranular spaces was measured to evaluate the supersaturation of the matrix. The measured Fe concentration is nearly below the resolution limit. The Sc concentration in particles that are not Sc-rich clusters is lower than in the surrounding matrix, indicating a parasitic increase in the surrounding background of the alloying-element-rich primary phase precipitates, which causes the increased contrast in Sc maps. Cu is highlighted because it is essential for strengthening during further processing and has a lower diffusion coefficient than the other two strengthening elements – Li and Mg [35]. The Cu concentration in the matrix is the same for both materials – 0.8 wt.% (Table 2). Areas of EDS measurements are highlighted in Figure 3.

The average spacing between particles and the volume fractions of primary phase precipitates are determined from lower magnification images (Figures 3,4). The DAS is measured as a tip-to-tip distance between two Al matrix dendrites, although the order of the dendrites is not specified. This DAS measurement method tends to give slightly lower values compared to methods that count the number of secondary dendrites along a primary dendrite [36]. Still, it remains valid when applied consistently across all studied materials. DAS is calculated from ten measurements. Although we reference the formation of eutectic cells in relation to the distribution of phases, the solidification of the α-Al phase is still assumed to be dendritic. Measurements of α-Al dendrite spacing in low-alloyed Al-based systems have previously been used to estimate solidification rates according to equation (2) [27,37]. Volume fractions of particles are computed using the linear intercept method and the Tomkeieff equation [38], which defines the volume fraction f of particles as:

$$f = 2N_i L, \tag{5}$$

Where:

N_i…The number of intercepted phases per unit line length,

L…The length of the intercepted particle segment.

Twenty lines were used for each volume fraction measurement. Intercepts are measured manually from a set of straight lines arranged in an evenly spaced perpendicular grid over SEM images. The measured DAS of the two alloys is similar within error, with (45 ± 8) μm for the MCA and (58 ± 6) μm for the MCB materials. Volume fractions of the primary phases evaluated by SEM (Figure 4) are 4.8% and 5.1% for the MCB and MCA materials, respectively.

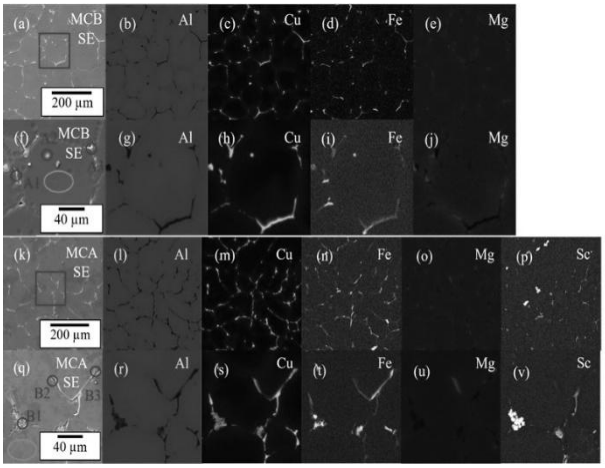

Fig. 3 *EDS mapping of MCB (a-j) and MCA (k-v) materials; SE images (a,f,k,q), Al (b,g,l,r), Cu (c,h,m,s), Fe (d,i,n,t), and Mg (e,j,o,u) maps for both materials in lower magnification (a-e, k-p) and closeups of highlighted sections (f-j,q-v); Sc distribution maps for the MCA material and highlighted section (p,v); Grey ovals without labels highlight areas of EDS measurements of matrix concentrations; Grey ovals with labels highlight areas of particle point analyses*

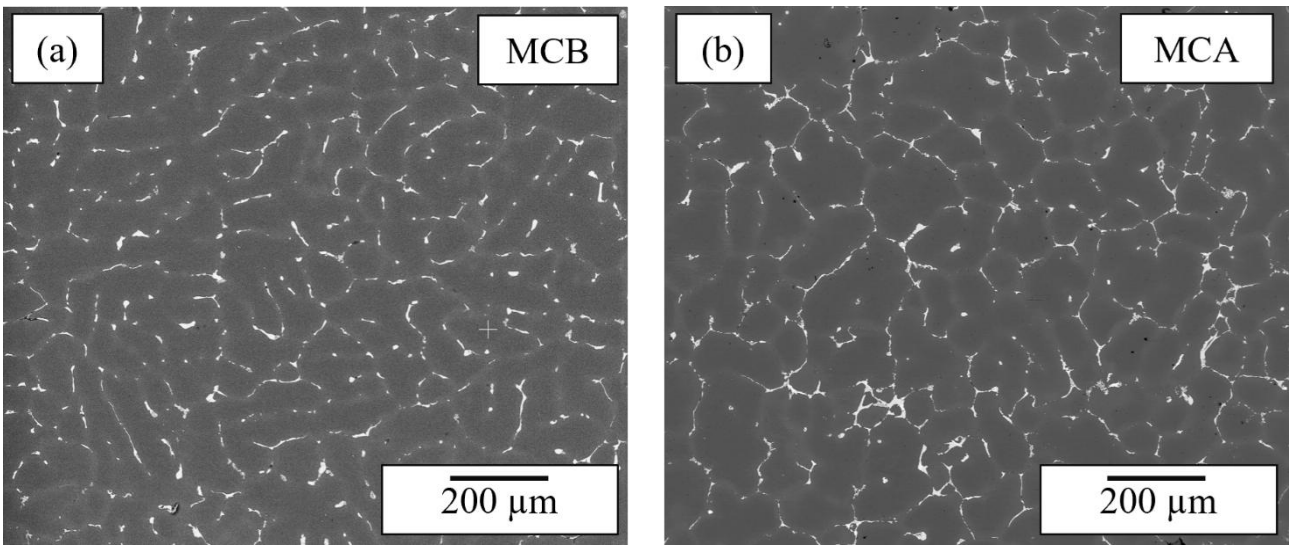

Fig. 4 *BSE images of primary phase distribution in random sections of the MCB (a) and MCA (b) material*

Tab. 2 *EDS point analyses of particles and areas of the Al matrix highlighted in Figure 4 (f,q); Values in wt. %*

	Cu	Fe	Mg	Sc
A1	9.5	0.1	2.3	-
A2	31.9	1.0	1.4	-
A3	31.8	0.2	1.8	-
MCB matrix	0.8 ± 0.1	< 0.1	0.9 ± 0.2	-
B1	23.6	2.7	0.9	8.5
B2	20.9	3.6	1.6	0.2
B3	20.3	0.1	4.4	0.1
MCA matrix	0.8 ± 0.1	< 0.1	1.0 ± 0.2	0.6 ± 0.2

The methods and measurements of grain size, DAS, constituent size, and constituent volume fraction were also used in studies of the twin-roll cast and melt-spun alloys.

3.2 Twin-roll casting

Orientation maps of 1 mm broad cross sections for both twin-roll cast materials were taken in the rolling direction (RD)/normal direction (ND) plane (Figure 5). Orientations are color-coded according to the triangle shown in Figure 5. A single average grain size for the entire strip could be misleading due to the presence of several different zones. Therefore, the circular intercept method was applied in three distinct regions: near the surface, halfway between the surface and the center, and at the center. These regions are called Areas 1, 2, and 3 (Figure 5). The measured grain sizes of both alloys increase from Area 1 to Area 2 but then decrease again in Area 3 (Table 3).

EDX mapping of the primary phase precipitates in the TRC materials reveals the formation of the eutectic θ(Al_2Cu) phase and a ternary Al_7Cu_2Fe phase (Figure 6, Table 4). The increased Mg concentration suggests the presence of the S(Al_2CuMg) phase. These phases were previously identified in these materials as reported by Cieslar et al. and Kralik et al. [34,39]. No W($Al_{8-x}Cu_{4+x}Sc$) precipitates or Sc-rich particle clusters appear in this material (Figure 6 (p,v), Table 4). Primary phases exclusively form along boundaries of eutectic cells, creating continuous polygonal segments in the observation plane (Figure 7), with individual segments being (5 ± 2) μm long and (1.0 ± 0.5) μm wide. The volume fraction of phases decreases only slightly and does not significantly change between the surface and the center of the strip. The average volume fraction of primary phases is 4.4 % and 4.3 % for the TRCB and TRCA materials, respectively. The primary phase size does not differ between the two alloys.

Due to the variance in solidification rates across the strip thickness, the DAS is individually evaluated in Areas 1, 2, and 3 (Figures 7– (b-d) and (f-h)). The average DAS for each region is summarized in Table 3. The measured DAS increases by approximately 40 % from the surface to the center for both materials and is lower overall for the TRCA material. The concentration of the main alloying elements is the same within the experimental scatter across the strip in intragranular spaces (Table 3).

Tab. 3 *Dendrite arm spacing (DAS) and grain size (GS) of the two twin-roll cast materials in the three evaluated areas*

Area	TRCB DAS [μm]	TRCB GS [μm]	TRCA DAS [μm]	TRCA GS [μm]
Area 1	6.5 ± 0.3	102 ± 14	5.7 ± 0.8	81 ± 8
Area 2	7.4 ± 0.5	152 ± 11	7.8 ± 0.9	128 ± 31
Area 3	9.4 ± 0.8	64 ± 6	8.6 ± 0.6	90 ± 3

Tab. 4 *EDS analyses of the selected primary phase precipitates from Figure 6 (f,q) and matrix concentrations in the three studied areas*

	Cu	Fe	Mg	Sc
A1	18.4	0.6	2.7	-
A2	27.1	2.2	2.1	-
A3	17.4	1.3	1.6	-
TRCB	1.1 ± 0.2	< 0.1	1.0 ± 0.3	-
TRCB (Area 2)	1.0 ± 0.2	< 0.1	1.0 ± 0.2	-
TRCB (Area 3)	1.0 ± 0.1	< 0.1	0.9 ± 0.3	-
B1	11.6	0.5	1.4	0.5
B2	8.5	1.7	1.1	0.4
B3	17.6	0.4	1.8	0.4
TRCA (Area 1)	1.2 ± 0.2	< 0.1	0.9 ± 0.2	0.7 ± 0.2
TRCA (Area 2)	1.1 ± 0.2	< 0.1	1.2 ± 0.3	0.6 ± 0.1
TRCA (Area 3)	1.1 ± 0.1	< 0.1	0.8 ± 0.1	0.7± 0.3

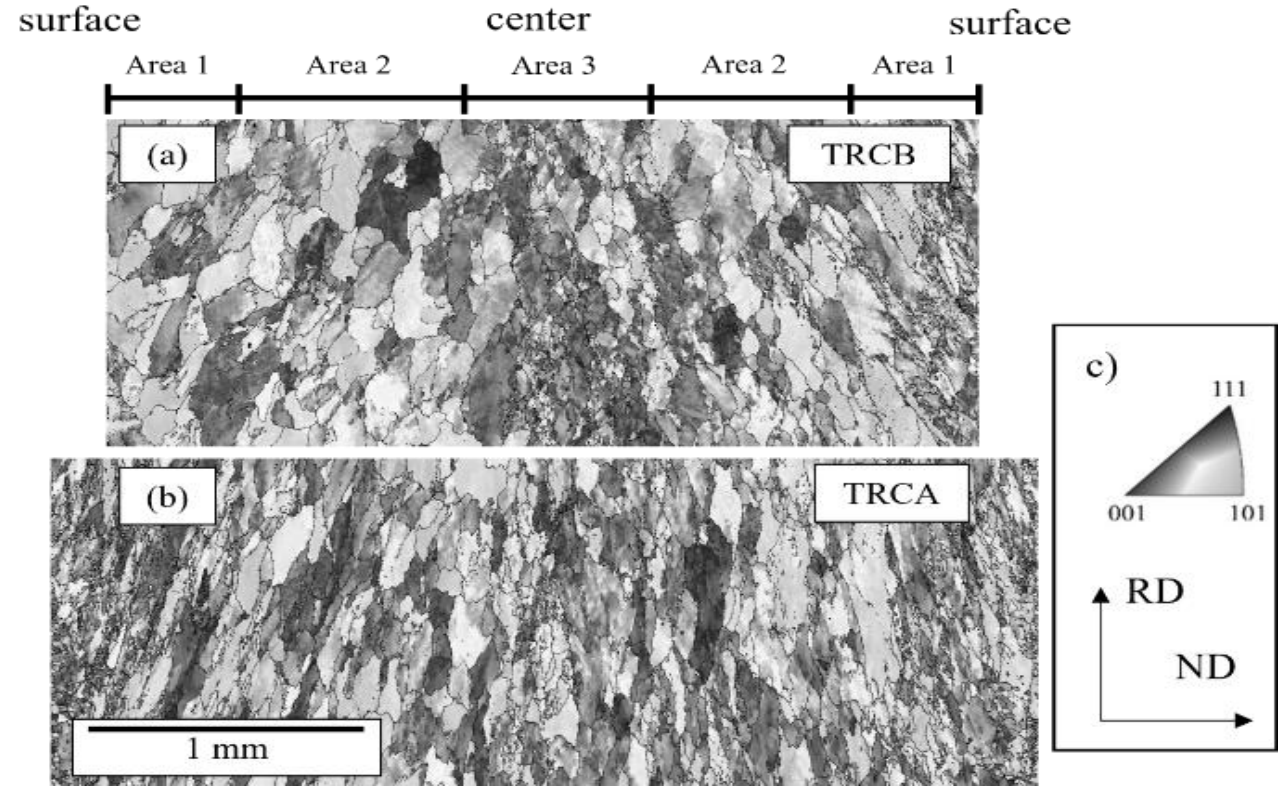

Fig. 5 *IPF maps of surface-to-surface cross sections of the TRCB (a) and TRCA (b) strips evaluated from the transversal direction (TD); IPF triangle of the orientation color coding; Rolling direction (RD) of the strip during casting and normal direction (ND) of the strip surface*

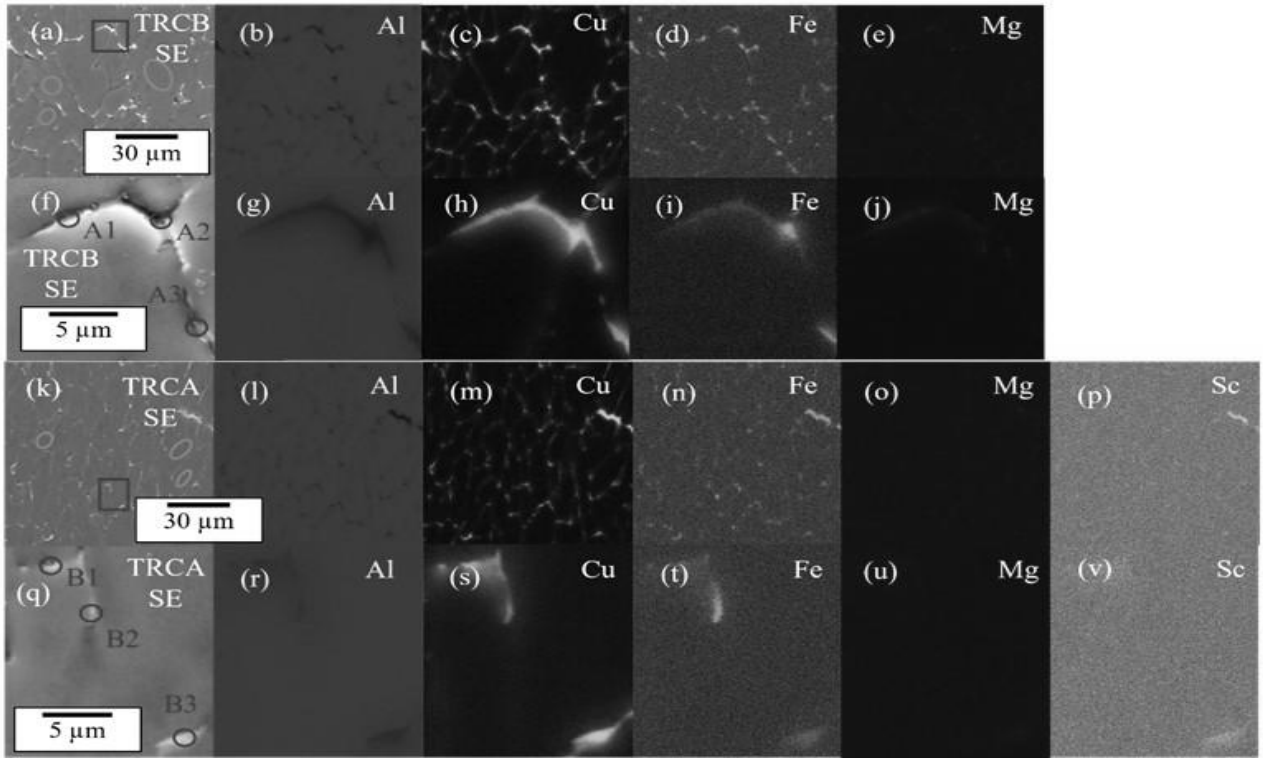

Fig. 6 *EDS mapping of the T (a-j) and TRCA (k-v) materials; Analysis performed in Area 2; SE images (a, f, k, q), Al (b, g, l, r), Cu (c, h, m, s), Fe (d, i, n, t), and Mg (e, j, o, u) maps for both materials (a-e, k-o) and closeups of highlighted sections (f-j, q-u); Sc distribution maps for the TRCA material (p) and the highlighted closeup section (v); Gray ovals without labels highlight areas of matrix concentration measurements in Area 2 of the TRC strips; Gray ovals with labels highlight particles for point EDS analyses*

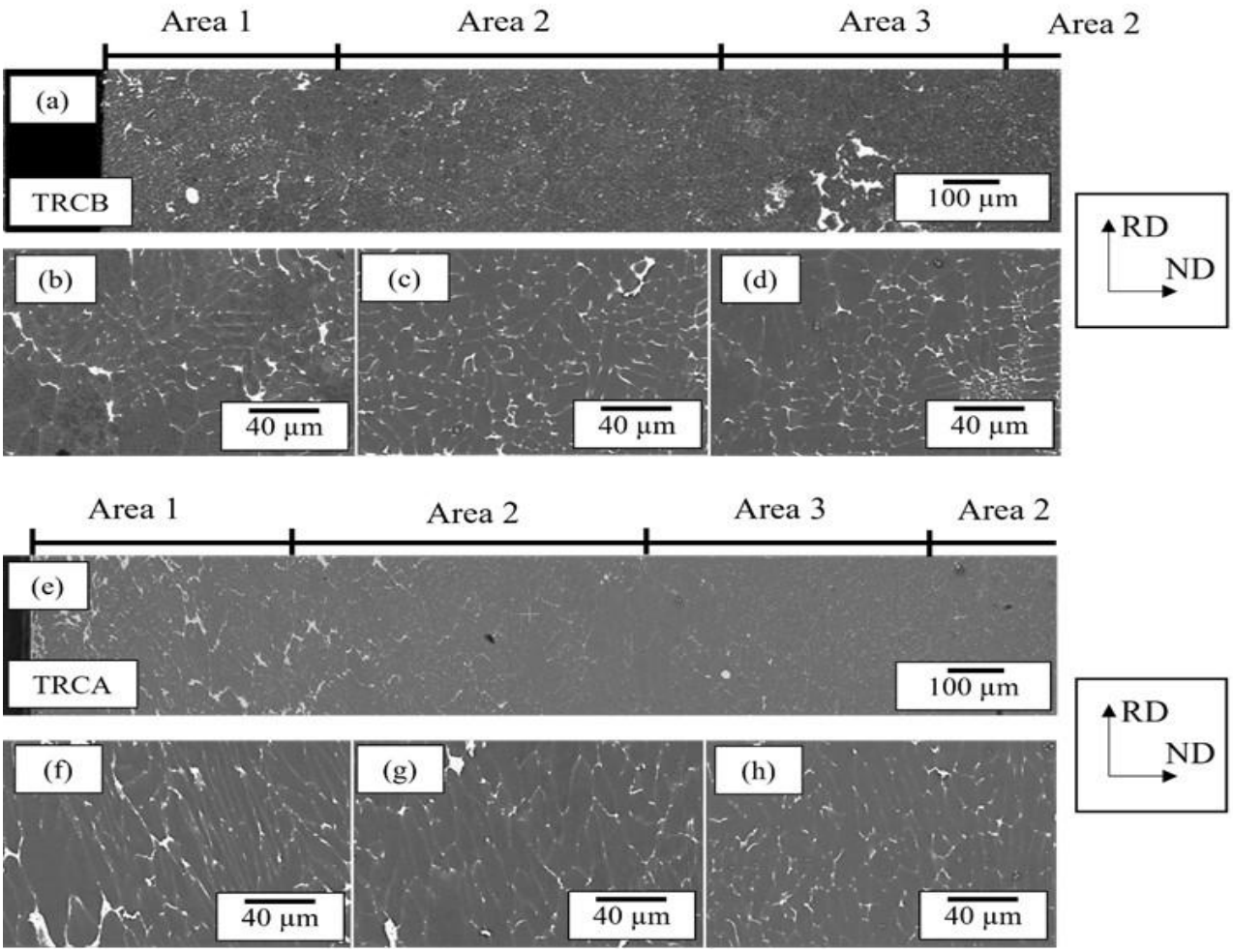

Fig. 7 *BSE images of the T (a-d) and TRCA (e-h) materials particle distribution observed from the transversal direction (TD); Low magnification overview images of the strip (a, e), closeups of the three areas – strip surface (Area 1) (b, f), area halfway between the surface and the center (Area 2) (c, g), and center of the strip (Area 3) (d, h)*

3.3 Melt-spinning

The contact side of the melt-spun strips develops tiny surface grains, followed by columnar grains perpendicular to the roll surface (Figure 8). Due to casting process instability, the strip thickness varies between 15 µm and 60 µm. Equiaxed grains (Zone 3) form at a certain distance from the roll. The circular intercept method is used in the columnar and equiaxed regions to calculate grain sizes, as shown in Table 5.

The local solidification regime determines the distribution of primary phase particles. A macroscopic featureless region (Gusakova et al. [24,25]) is not clearly observed in the melt-spun alloys (Figure 9 – (b, f)). The columnar regions contain spherical precipitates inside individual grains. Near the contact surface, these phases have a diameter of (50 ± 7) nm, while near the threshold between columnar and equiaxed structures, they have a diameter of (150 ± 40) nm. The volume fraction of primary phases varies significantly from the surface or roll interface toward the equiaxed part of the strips. The surface area contains only 1.7% volume fraction of primary phases, increasing to 2.8% in the columnar region and 4.1% in the equiaxed section of the strip. The measured volume fractions of primary phases are consistent across both alloys.

EDS maps of areas near the surface of the strip reveal two types of phases: more rounded, Cu-rich phases, likely the stable θ phase, and rod-like Cu and Fe-containing phases, probably the Al_7Cu_2Fe phase (Figure 10). No significant Sc segregation is observed in the MSA material. DAS can only be determined in the equiaxed region (Table 5) since it is the only part of the material formed by dendritic growth [24,25].

Tab. 5 *DAS in Zone 3 of the melt-spun strips (Figure 9 (d,h)), and columnar (Figure 8 Zone 2) and equiaxed (Figure 8 Zone 3) grain sizes of the strips*

Area	MSB DAS [µm]	MSB GS [µm]	MSA DAS [µm]	MSA GS [µm]
Columnar	-	9.2 ± 1.7	-	7.3 ± 0.4
Equiaxed	0.6 ± 0.2	7.7 ± 1.4	0.6 ± 0.1	7.3 ± 0.6

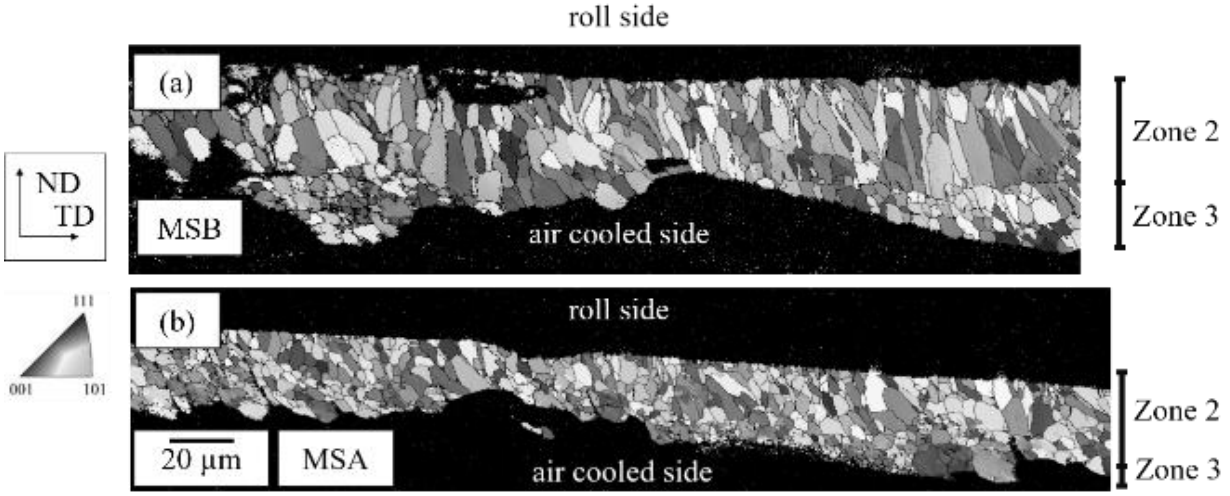

Fig. 8 *IPF maps of the MSB (a) and MSA (b) materials cross sections from the surface/roll interface (top) to the air-cooled side of the strip (bottom) analyzed from the rolling direction (RD); Zone 1 is not clearly evident in EBSD measurements; Zones 2 and 3 are highlighted in the materials*

The matrix concentration of solutes in the melt-spun materials is higher than in previous casting types but varies across the melt-spun strips. Both materials show similar matrix concentrations in the evaluated regions. EDS analyses of selected particles and matrix concentrations in the highlighted zones are summarized in Table 6. The analyzed particles include boundary particles in the equiaxed region (particles A1, A2, B1, B2 in Figure 9 (d,h)), spherical particles in the columnar region (particles A3, B3 in Figure 9 (c,g)), boundary particles in the columnar region (particles A4, B4 in Figure 9 (c,g)), and two particles near the surface/roll interface (A5, A6, B5, B6 in Figure 10). EDS analyses performed in SEM and STEM show increased Fe content in the primary phases, indicating the presence of Al_7Cu_2Fe precipitates. Mg content in the selected phases is not higher than in the matrix for either SEM or STEM. STEM and SEM-EDS analyses cannot be directly compared because the information depth of the SEM beam exceeds the particle size. Therefore, the SEM point EDS spectra are largely influenced by the surrounding Al matrix.

Tab. 6 *EDS analyses of the melt-spun materials; Average concentrations of alloying elements in the three studied zones (Figure 10) and point spectra of selected particles (Figure 9,10); All values are in wt. %*

			Cu	Fe	Mg
MSA	Matrix	Zone 1	1.4 ± 0.1	0.3 ± 0.2	0.8 ± 0.1
		Zone 2	2.1 ± 0.3	0.6 ± 0.2	1.1 ± 0.1
		Zone 3	2.5 ± 0.3	0.5 ± 0.1	1.2 ± 0.2
	Particle	A1	11.1	1.2	1.0
		A2	9.8	1.0	1.3
		A3	8.3	0.6	1.0
		A4	6.0	1.0	1.0
		A5	44.0	2.5	0.1
		A6	56.9	0.4	0.0
MSB	Matrix	Zone 1	1.2 ± 0.2	0.3 ± 0.1	1.0 ± 0.1
		Zone 2	2.2 ± 0.2	0.7 ± 0.2	1.0 ± 0.3
		Zone 3	2.6 ± 0.3	0.4 ± 0.1	0.9 ± 0.1
	Particle	B1	12.9	0.9	1.2
		B2	14.0	0.7	1.1
		B3	19.0	1.4	1.1
		B4	16.5	3.4	1.1
		B5	59.2	0.8	0.0
		B6	34.7	5.0	0.0

ISSN 1213–2489
e-ISSN 2787–9402

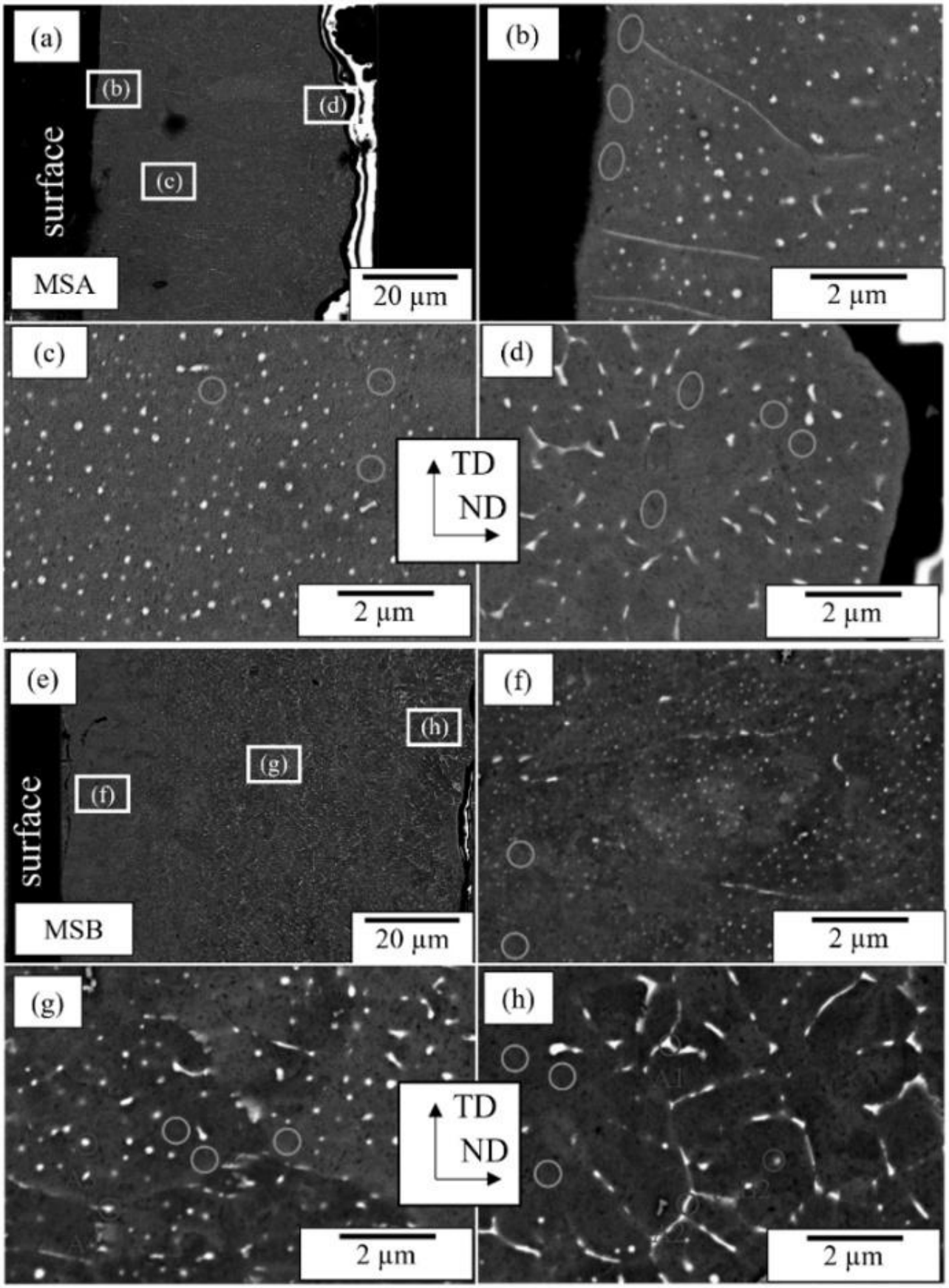

Fig. 9 *BSE images of the MSB (e-h) and MSA (a-d) strips observed from the rolling direction (RD); Cross sections of strips (a, e) and higher magnification images of selected sections close to the surface/roll interface (b, f), in the columnar area (c, g), and the dendritically solidified regions (d, h); EDS analyses of the highlighted particles (gray circles A1-4, B1-4) are shown in Table 6; gray circles without labels are areas of matrix concentration measurements*

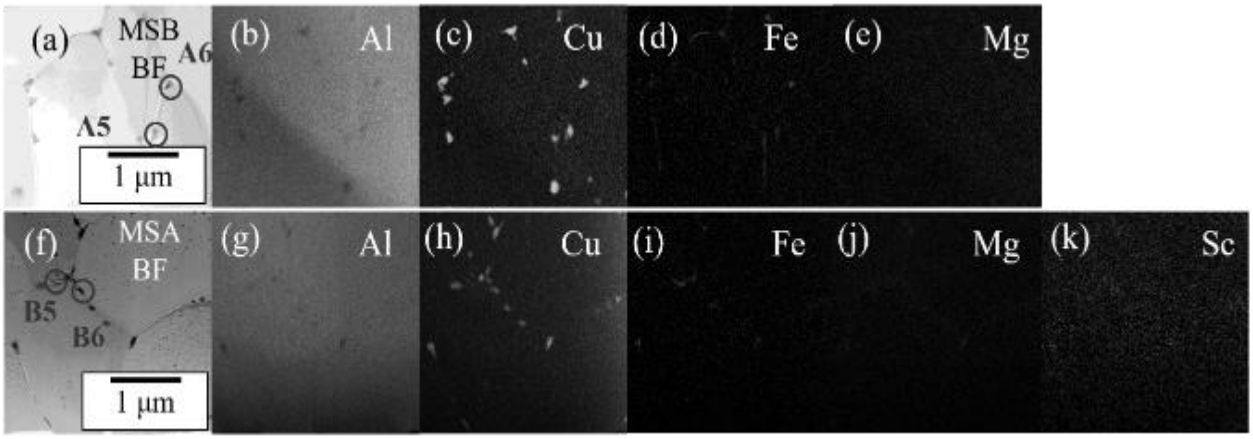

Fig. 10 *EDS mapping of the MSB (a-e) and MSA (f-k) strips close to the surface/roll interface; STEM BF micrographs of the mapped MS (a) and MSA (f) material areas; Element distribution maps for Al (b, g), Cu (c, h), Fe (d, i), and Mg (e, j) in both materials; Sc distribution map (k) in the MSA materiál; Selected particles are used for measuring alloying element concentrations (A5, A6, B5, B6 – grey circles)*

4 Discussion

4.1 The influence of Sc addition

Sc-rich clusters can pin grain boundaries in the MCA material (Figure 3 (b)). However, their number is too low to cause significant grain refinement during the casting process. Both grain size and DAS of the twin-roll cast and melt-spun materials are consistently lower in alloy A than in alloy B. While this difference is often within the experimental scatter of the measured values, a refining effect of Sc on DAS has been previously observed, including Zr-containing Al-Cu-based alloys [40,41]. However, the results from our study remain inconclusive in this regard.

4.2 Solidification rate determination

Solidification rates associated with different casting methods were calculated from dendrite spacing where possible. The values of n and A (Equation 2) were calculated within the limits established in an Al-Cu-based alloy dendrite spacing review by Eskin et al. [27]. They estimated the value of n as fixed at 0.33 and determined new A coefficients for alloys with 2.12 (A=84) and 3.24 (A=101) wt. % Cu. Based on their coefficients, we will use their fixed value of n and an interpolated value of A = 93. These values ignore the influence of Zr and Sc on DAS. While these additions have a strong influence over grain structure (Xu et al. [42] reported an order of magnitude difference of grain size in Al-Mg-Si-based alloys), their influence on SDAS is significantly lower (Xu et al. [42] around a 25 % decrease in SDAS, Prach et al. [43] less than 20 % in an Al-Mg-Si-Mn-based alloy). A summary of the DAS for individual casting method/alloy/area combinations, along with the corresponding calculated solidification rates, is presented in Table 7.

Tab. 7 *Solidification rate estimated from Equation (2)*

Material (area)	DAS [µm]	V [K·s^{-1}]
MCB	45 ± 8	(9.0 ± 0.3)
MCA	54 ± 6	(5.0 ± 0.3)
TRCB (Area 1)	6.5 ± 0.3	(3.1 ± 0.2)x10^3
TRCB (Area 2)	7.4 ± 0.5	(1.8 ± 0.2)x10^3
TRCB (Area 3)	9.4 ± 0.8	(1.0 ± 0.1)x10^3
TRCA (Area 1)	5.7 ± 0.8	(4.7 ± 0.6)x10^3
TRCA (Area 2)	7.8 ± 0.9	(2.1 ± 0.2)x10^3
TRCA (Area 3)	8.6 ± 0.6	(1.5 ± 0.1)x10^3
MSB (Zone 3)	0.6 ± 0.2	(4.3 ± 1.3)x10^6
MSA (Zone 3)	0.6 ± 0.1	(5.4 ± 0.7)x10^6

Twin-roll cast and melt-spun materials exhibit a profile of varying solidification rates throughout the as-cast material. The observed DAS and calculated solidification rates for the twin-roll cast materials yield results similar to those in studies by Grydin et al. [26,44] on Al-based alloys produced on the same twin-roll caster. Based on solidification lengths (distance between the last fully melted and the first fully solidified part of the strip) in the caster, the solidification rate was estimated at 4500 $K \cdot s^{-1}$ at the surface and 2500 $K \cdot s^{-1}$ in the center. However, Grydin performed the casting with twice the casting rate and Cu shells, which have higher heat conductivity (330 $W \cdot m^{-1} \cdot K^{-1}$ [26]) than steel shells (20-60 $W \cdot m^{-1} \cdot K^{-1}$ [45]). This explains the discrepancy between the calculated absolute values of solidification rates for our materials and the model estimated by Grydin.

The solidification rate profile for the melt-spun alloy cannot be determined through DAS measurements alone, but can be calculated using the general one-dimensional diffusion equation:

$$\frac{\partial T}{\partial t} = \alpha \frac{\partial^2 T}{\partial x^2} = \frac{k}{C\rho} \frac{\partial^2 T}{\partial x^2}, \quad (6)$$

Where:

t…Time,

x…The distance from the surface/roll interface,

a…Thermal diffusivity,

k…Thermal conductivity,

C…Specific heat capacity,

T…Thermodynamic temperature,

ϱ…The density of the alloy [46].

The solution of Equation (6) can be written as:

$$T(x,t) = K_1 + K_2 \operatorname{erf}\left(\frac{x}{2\sqrt{\alpha t}}\right), \quad (7)$$

Where:

K_1 and K_2…Constants dependent on boundary conditions [45].

Applying boundary conditions of the ribbon and the Cu wheel and assuming a constant solidification rate, which is justified by the very short solidification time expected for the melt-spun strips, leads to an equation for solidification time:

$$t = \frac{\delta_1^2 \pi (C_1 \rho_1)^2}{k_2 C_2 \rho_2}, \quad (8)$$

Indexed parameters with 1 and 2 are the ribbon and Cu wheel constants, respectively. δ_1 is the ribbon thickness. The density and heat capacity of the alloy are 2300 $kg \cdot m^{-3}$ and 1230 $J \cdot kg^{-1} \cdot K^{-1}$, respectively [26]. The density and heat capacity of a copper wheel are 8900 $kg \cdot m^{-3}$ and 384 $J \cdot kg^{-1} \cdot K^{-1}$, respectively. The thermal conductivity of a copper wheel is 400 $W \cdot m^{-1} \cdot K^{-1}$ [46]. The thickness of the studied strips can vary, but areas that include the dendritic growth zone range from 30 μm to 60 μm in thickness. This corresponds to a solidification time between 16 μs and 66 μs.

The solidification rate at a certain distance from the copper wheel could be further estimated. The equation is essentially a function of $(1/\delta^2)$ of ribbon thickness.

$$V(x) = \frac{-\alpha_1 \exp\left(-\frac{C_2 k_2 \rho_2}{4\pi C_1 k_1 \rho_1}\right)\left(-T_{10} + \frac{k_1\sqrt{\alpha_2}T_{10} + k_2\sqrt{\alpha_1}T_{20}}{k_1\sqrt{\alpha_2} + k_2\sqrt{\alpha_1}}\right)}{2x^2\pi^2\left(\frac{C_1 k_1 \rho_1}{C_2 k_2 \rho_2}\right)^{3/2}}, \quad (9)$$

T_{i0} is the initial temperature of the melt/roll, which is 1273 K and 300 K, respectively; thermal diffusivities are 3.6×10^{-5} $m^2 \cdot s^{-1}$ and 1.2×10^{-4} $m^2 \cdot s^{-1}$ for the alloy and roll, respectively [46]. The thermal conductivity of the alloy is 88 $W \cdot m^{-1} \cdot K^{-1}$ [26]. The plot of solidification rates calculated by this equation is shown in Figure 11. The spread of solidification rates in the melt-spun materials is much higher than that throughout the twin-roll cast strip, changing by two orders of magnitude from the surface to the thickest parts of the ribbon.

An obvious issue with this model is that the solidification rate approaches infinity at the surface/roll interface. However, it provides reasonable results for thicknesses of tens of micrometers. By measuring the real thickness at which the DAS measurement was performed in the equiaxed region, we can compare the DAS model results with the diffusion-based calculation results. The results are visualized in Figure 11 and summarized in Table 8, confirming a good agreement between the two approaches.

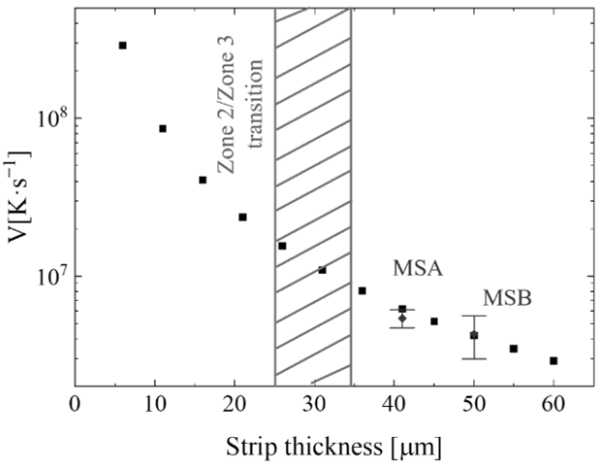

Fig. 11 *The plot of the solidification rate profile with varying ribbon thickness was calculated according to Equation (9); Thicknesses of observed Zone 2/Zone 3 transitions in Figures 8 and 9 are highlighted in hatched area; DAS-based solidification rate measurements in Zone 3 of the MSB and MSA materials (Figure 9 (d,h))*

Tab. 8 *Comparison of solidification rate estimates according to DAS measurements and calculations through Equation (2) and diffusion-based Equation (9)*

Material	DAS measurement thickness [μm]	DAS-based V [K·s^{-1}]	Diffusion-based V [K·s^{-1}]
MSB	50	(4.3 ± 1.3)x10^6	4.2x10^6
MSA	41	(5.4 ± 0.7)x10^6	6.2x10^6

While the diffusion-based estimate for the MSA alloy is slightly higher, the estimates for the MSB alloy are in surprisingly good agreement

4.3 Grain structures

The nonlinear relationship between grain size and solidification rate in different parts of the TRC strips (Equation 3) is not maintained. This is due to centerline segregation, which causes the formation of coarse constituent phases that hinder grain growth [47]. To provide a rough estimate, an average grain size and solidification rate are used for the plot. Plotting the measured average grain size for each alloy against the estimated solidification rates yields parameters B and m, as shown in Table 9 and Figure 12. Figure 12 also compares our data with literature references [9-11,14], which exhibit similar behavior to that of our alloys.

Tab. 9 *Parameters of the relation between average grain size and solidification rate according to Equation (3) for both alloys*

	mold-cast GS [μm]	twin-roll GS [μm]	melt-spun GS [μm]	B [μm·s^m·K^{-m}]	m
Alloy B	156 ± 11	115 ± 11	8.7 ± 1.6	345 ± 36	0.22
Alloy A	131 ± 17	99 ± 13	7.3 ± 0.7	292 ± 31	0.22

The *m* parameters agree with those stated by Eskin et al. [27] for Al-Cu alloys. Parameter B is lower in order of magnitude than the values that Eskin et al. [27] determined in binary Al-Cu alloys owing to the addition of Zr and Sc, which significantly decrease grain size [48,49]. The average B parameter is lower for alloy A but is the same within the experimental error.

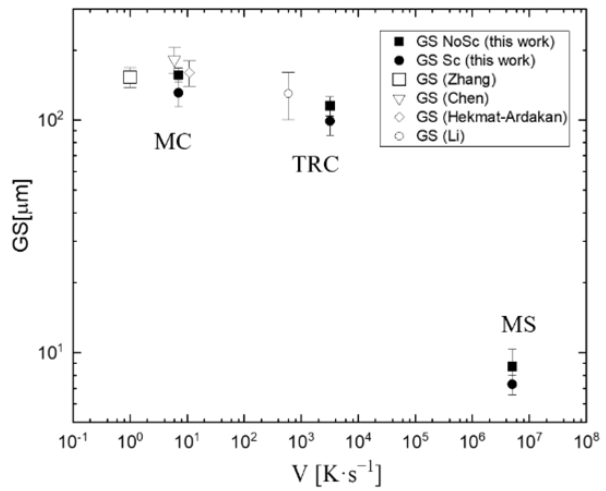

Fig. 12 *The plot of measured grain size versus the average solidification rate calculated from Equation (2) for the mold-cast and twin-roll cast alloys and the dendritically solidified part of the melt-spun alloy; Data received in this work are shown as full symbols, and the literature data [9-11,14] are demonstrated as empty symbols*

Heat is evenly extracted from all sides of the mold-cast ingot during cooling. Additionally, no external forces are applied to the ingot during solidification and cooling, which results in the formation of an equiaxed structure. The as-cast structures we observe in our materials match those observed by Hekmat-Adrakhan et al. [9] in terms of constituent particle size, grain sizes, and DAS.

TRC materials are partially rolled [12]. The effect of rolling is more pronounced closer to the surface of the strip, resulting in a gradient microstructure with elongated or columnar grains at the surface, depending on the efficiency of heat transfer and applied forces, and more equiaxed grains in the center [26,31].

Columnar grains in the melt-spun materials result from cellular crystallization and unidirectional heat transfer between the spinning roll and the solidified ribbon. Columnar grains are a characteristic of this cooling mechanism, regardless of the solidification rate. Flemings [29] states that such a mechanism is possible with a sufficiently high *G*/*R* ratio (Equation (1) describes the thermal gradient at the solid/liquid interface and the velocity of the dendrite tip/solidification interface). A high *G*/*R* ratio is reached by adding heat at one end and extracting it from the other.

The shift to equiaxed growth occurs at lower crystallization speeds, as more heat is extracted from the melt-spun ribbon/air interface, further from the water-cooled roll, at higher thicknesses, thus decreasing the *G*/*R* ratio. Additionally, the specific alloy composition affects the size of the columnar zone and the transition to equiaxed grains. EBSD results (Figure 8) indicate that the transition to columnar growth occurs consistently at comparable thicknesses for the

studied alloys, approximately 30 μm. This corresponds to a decrease in solidification rate below 10^7 K·s^{-1} based on diffusion-based solidification rate estimates (Figure 11). Since diffusionless solidification is associated with a high velocity of the solidification front, we can estimate this velocity based on the solidification time in Equation (7) for ribbon thickness between 25 and 35 μm. The corresponding solidification time is between 23 and 13 μs, and the solidification velocity is between 1.5 and 2.0 m·s^{-1} (Figure 13).

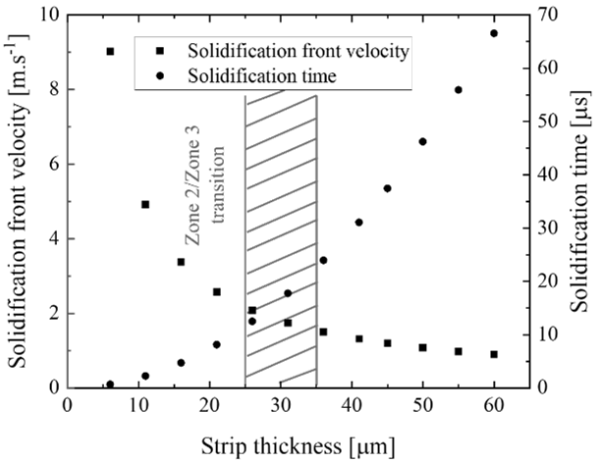

Fig. 13 *Theoretical variance of solidification velocity and time with melt-spun strip thickness; The hatched region highlights the critical thickness of the transition between cellular solidification in Zone 2 and the dendritic solidification in Zone 3*

4.4 Constituents, Cu concentration

Constituent phase particles show significant refinement with increasing solidification rate during casting. Their particle size, measured by particle thickness, decreases threefold from mold-cast to TRC materials, then diminishes by another order of magnitude between TRC and melt-spun materials. The precipitate sizes in the mold-cast alloys are comparable to those in standard AA2195 DC-cast alloys as observed by Hekmat-Ardakan et al. [9]. Similarly, early studies on Al-Cu-Li-based TRC alloys by Li et al. [14] reveal similar particle sizes (around 1 μm) and comparable particle distributions. Melt-spun materials contain coarser boundary phases and finer spherical precipitates within the grains. The boundary precipitate size increases slightly along the strip, from about (100 ± 30) nm near the surface/roll interface to (140 ± 40) nm in the columnar and equiaxed regions. Conversely, the spherical precipitates grow from (50 ± 7) nm at the surface/roll interface to (150 ± 40) nm in the columnar zone, reaching sizes comparable to the boundary phases. These spherical phases are evenly distributed in the as-cast columnar grains. No spherical precipitates are found inside grains in the equiaxed regions due to dendritic growth, which segregates alloying elements to the eutectic cell boundaries, resulting in a low driving force for precipitate formation within the cells. Particle sizes and volume fractions across different materials are summarized in Table 10. Average values for both alloys are used in the plot in Figure 14, as their differences are smaller than the experimental scatter. The spherical particle diameter characterizes zones 1 and 2 of the melt-spun strips (Figure 9 (b,c,f,g)) to examine how constituent phase sizes vary with the high cooling rates in these zones.

Studies on rapidly solidified Al-Cu-Li-Mg-Zr-based materials suggest that the boundary phases share the same structure as those formed at lower solidification and cooling rates [3,19,50]. EDS analyses summarized in Table 5 reveal the presence of the binary θ(Al_2Cu) phase in both boundary phases and spherical precipitates. An increased Fe content compared to the surrounding matrix indicates the formation of the Al7Cu2Fe phase. The presence of the Al_7Cu_2Fe phase is also confirmed in particles B4, B6, and A5 (Figure 9 (a,e), Figure 10 (a)). The higher Fe content observed in the TEM analyses results directly from the lower contribution of the surrounding matrix, which has a low Fe concentration. Mg content in the analyzed phases never exceeds the average values of the surrounding matrix, indicating that Mg-containing constituents do not form.

The relationship between the cooling rate of the alloys and Cu concentration in the matrix is highly nonlinear. The MC alloys have Cu concentrations in the matrix of around 0.8 wt. % for both alloys, which is still substantially higher than the equilibrium solubility limit—0.35 wt. % for Cu in Al [51]. Such concentrations are relatively common even in standard direct-chill cast materials, as evidenced by Wang et al. [50], who observed about a third of the Cu content in the supersaturated matrix. Increasing the cooling rate to levels of TRC, around 1.0 wt.% in both TRC materials, does not significantly increase supersaturation. This aligns with results obtained by Li et al. [14] in their Al-Cu-Li-based TRC materials. Dendritic regions of the melt-spun alloys contain slightly higher concentrations of Cu—1.2 wt. % and 1.4 wt. % for the MSB and MSA materials, respectively. Gianogolio et al. [22] report similar Cu concentration variations in their study of atomized particles formed with solidification rates between 102 K·s^{-1} and 105 K·s^{-1}. They measured a range of Cu concentration from 1.1 wt. % to 1.4 wt. % in an alloy containing 2.4 wt. % Cu.

Increasing the solidification rate beyond 10^7 K·s^{-1} introduces a shift in the solidification mode, causing a sharp increase in the matrix solute concentration (Table 10). Due to this sharp change, the dendritic solidification regime results, such as the DAS and grain size relations, cannot be extrapolated to the columnar and featureless regions of the melt-spun strips.

Tab. 10 *Particle sizes, volume fractions, and Cu concentrations for both alloys prepared by different casting methods*

		w [μm]	f [%]	Cu concentration [wt. %]
MCB		3.2 ± 1.4	4.7 ± 0.4	0.8 ± 0.2
MCA		2.9 ± 1.6	5.2 ± 0.3	0.8 ± 0.2
TRCB	Area 1	1.1 ± 0.5	4.6 ± 0.4	1.1 ± 0.2
	Area 2	1.2 ± 0.4	4.6 ± 0.3	1.0 ± 0.2
	Area 3	1.4 ± 0.5	4.1 ± 0.3	1.0 ± 0.1
TRCA	Area 1	1.3 ± 0.4	4.3 ± 0.5	1.2 ± 0.2
	Area 2	1.1 ± 0.2	4.7 ± 0.4	1.1 ± 0.2
	Area 3	1.3 ± 0.5	4.4 ± 0.2	1.1 ± 0.1
MSB	Zone 1	0.05 ± 0.01	1.8 ± 0.4	1.4 ± 0.1
	Zone 2	0.11 ± 0.03	3.1 ± 0.4	2.1 ± 0.3
	Zone 3	0.13 ± 0.05	4.0 ± 0.5	2.5 ± 0.3
MSA	Zone 1	0.04 ± 0.01	1.6 ± 0.3	1.2 ± 0.2
	Zone 2	0.11 ± 0.02	2.6 ± 0.5	2.2 ± 0.2
	Zone 3	0.16 ± 0.06	4.2 ± 0.4	2.6 ± 0.3

A graph illustrating particle parameters—width, volume fractions, and Cu concentration in the matrix—is shown in Figure 14. A single average Cu concentration value is used for the plot across both alloys and the three studied TRC areas because the variation among individual values is smaller than the measurement scatter. The solidification rates for zones 1 and 2 of the melt-spun alloys are set at $3x10^8$ K·s^{-1} and $2x10^7$ K·s^{-1}, respectively, consistent with the plot in Figure 11. For comparison, particle sizes and Cu concentrations from selected studies are included in the same graph. Particle sizes and volume fractions follow a power law within the experimental scatter throughout the entire range of cooling rates. Cu concentrations reported by Gianoglio et al. [22] are consistently about 0.2 wt.% higher, but increase at a similar pace with increasing solidification rates.

Power laws similar to those in Equations (2 and 3) can be established for the remaining parameters. These power laws are defined as:

$$X = C_x V^{-j_x}, \tag{10}$$

Where C_x and j_x are material-dependent constants for each parameter x, where x is w, f, or Cu concentration. The calculated constants are summarized in Table 11.

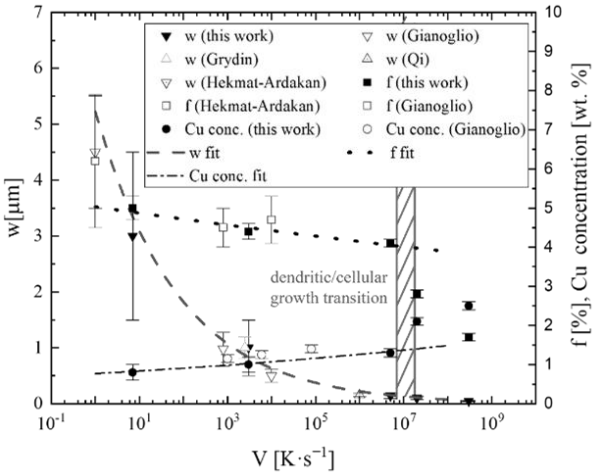

Fig. 14 *A plot of variance of structural parameters (particle volume fraction, Cu concentration, constituent phase width) with the calculated solidification rate; Points measured in this work (full black symbols) are fitted by general power functions in Equation (10); Data obtained from the literature [19,22,25] are represented by empty symbols*

Tab. 11 *Constants C_x and j_x from Equation (10) for the different studied microstructural parameters*

x	C_x	j_x
w	5.2	0.23
f	5.0	0.014
Cu conc.	0.8	0.036

The Cu concentration and volume fraction of primary phase particles exhibit opposite trends, with a sharp change in the columnar part of the melt-spun strips. A change in volume fraction relates to a change in Cu concentration in the matrix. The stoichiometric θ phase contains 1/3 Cu, meaning that one-third of the measured volume fractions of primary phases consist of Cu atoms. This estimate relies on two assumptions— that all primary phase particles are θ(Al2Cu) phases, and that differences between the unit cell

volumes of θ and the Al matrix are ignored. However, this rough estimate suggests up to 1.6 at.% Cu, while both materials contain only 1.1 at.% Cu overall. Sarreal and Abbaschian [52] showed that the θ phase could contain as little as 0.5 of the stoichiometric Cu content, which explains the discrepancy between the measured volume fraction of the θ(Al_2Cu) phase and the Cu concentration in the matrix.

5 Summary

A study of the as-cast structures of Al-Cu-Li-Mg-Zr-Sc alloys cast by three different casting methods was conducted. The solidification rate was determined to lie in the range of 1 $K \cdot s^{-1}$ to 10^8 $K \cdot s^{-1}$ using a combination of diffusion and empirical models. The following was confirmed:

- Grain size and dendrite arm spacing of materials formed with solidification rates between 1 $K \cdot s^{-1}$ and 10^7 $K \cdot s^{-1}$ follow simple power laws as described in Equations (2) and (9). In these solidification rate ranges, additional power laws were determined for Cu concentration, the constituent size, and volume fraction. Regular eutectic cells form in these solidification rate ranges. Higher solidification rates lead to the formation of materials with a lower dendritic spacing, smaller particle size, higher degree of supersaturation, and lower particle volume fraction.
- A critical solidification rate threshold is crossed during the solidification of the melt-spun strips. A higher solidification rate, closer to the water-cooled roll, leads to near-diffusionless solidification, resulting in a sharp increase in solute supersaturation and the formation of columnar grains in the melt-spun strips. The Cu concentration and the particle volume fraction no longer follow the power laws. The columnar areas of the melt-spun strips contain a fine dispersion of spherical θ(Al_2Cu) phase precipitates in addition to finer rod-shaped constituents observed at dendritic boundaries.
- The near-diffusionless solidification threshold was determined using diffusion models to be 10^7 $K \cdot s^{-1}$. The diffusion and empirical DAS-based models are in good agreement, and the solidification rate determined by these models for Zone 3 of the strips is the same within error.
- The effect of Sc is the highest in mold-cast materials, where the low solidification and cooling rate allow the formation of the detrimental W($Al_{8-x}Cu_{4+x}Sc$) phase. This phase no longer forms when higher solidification rates are applied in the TRC or melt-spun materials. The influence of Sc on the grain size and dendrite arm spacing cannot be reliably proven since the measured values are the same for both alloys within their experimental scatter.

Acknowledgement

The financial support of the Charles University Grant Agency project number 292522 are highly acknowledged.

References

[1] LAVERNIA, E. J, GRANT, N. J. (1987) Aluminium-lithium alloys. In: *Journal of Materials Science*, Vol. 22, pp. 1521-1589.

[2] WANG, S. C., STARINK, M. J. (2005) Precipitates and intermetallic phases in precipitation hardening Al–Cu–Mg–(Li) based alloys. In: *International Materials Reveiw*, Vol. 50, pp. 193-215.

[3] SURESH, M., SHARMA, A., MORE, A. M., NAYAN, N., SUWAS, S. (2018) Effect of Scandium addition on evolution of microstructure, texture and mechanical properties of thermo-mechanically processed Al-Li alloy AA2195. In: *Journal of Alloys and Compounds* Vol. 740, pp. 264-374.

[4] FINK, D., HNATOWICZ, V., KVITEK, J., HAVRANEK, V. ZHOU, J. T. (1992) External oxidation of aluminium-lithium alloys. In: *Surface and Coatings Technology* Vol. 51 , pp. 57-64.

[5] DENG, S., LIU, Z., ZHENG, G., XIANG, H., MA, P., YIN, J., KANG, L., WEN, S., LI, J., LIU, D. (2024) In: *Journal of Materials Science Technology* Vol. 192, pp. 42-53.

[6] CASSADA, W. A., SHIFLET, G. J., STARKE, E. A. (1991) Mechanism of AI2CuLi (T1) Nucleation and Growth In: *Metallurgical transactions: A* Vol. 22, pp. 287-297.

[7] XU, P., JIANG, F., TANG, Z., YAN, N., JIANG, J., XU, X., PENG, Y. (2019) Coarsening of Al3Sc precipitates in Al-Mg-Sc alloys In: *Journal of Alloys and Compounds* Vol. 781, pp. 209-215.

[8] NADELLA, R., ESKIN, D. G., DU, Q., KATGERMAN, L. (2008) Macrosegregation in direct-chill casting of aluminium alloys In: *Progress in Materials Science* Vol. 53, pp. 421-480.

[9] HEKMAT-ARDAKAN, A. ELGALLAD, E. M., AJERSCH, F., CHEN, X.-G. (2012) Microstructural evolution and mechanical properties of as-cast and T6-treated AA2195 DC cast alloy In: *Materials Science and Engineering: A* Vol. 558, pp. 76-81.

[10] ZHANG, F., SHEN, X., YAN, J., SUN, J., SUN, X., YANG, Y. (2014) Homogenization heat treatment of 2099 Al-Li alloy In: *Rare Metals* Vol. 33, pp. 28-36.

[11] CHEN, K., LI, Z., PAN, S. (2022) Effect of composition on microstructure and properties of as-cast 2196 Al–Cu–Li alloy In: *Materials Science and Technology Series* Vol. 38 , pp. 1168-1184.

[12] BAREKAR, N. S., DHINDAW, B. K. (2014) Twin-Roll Casting of Aluminum Alloys – An Overview In: *Materials and Manufacturing Processes* Vol. 29, pp. 651-661.

[13] SLAMOVA, M., KARLIK, M., ROBAUT, F., SLAMA, P., VERON, M. (2002) Differences in microstructure and texture of Al–Mg sheets produced by twin-roll continuous casting and by direct-chill casting In: *Materials Characterization* Vol. 49, pp. 231-230.

[14] LI, S., HE, C., FU, J., XU, J., XU, G., WANG, Z. (2020) Evolution of microstructure and properties of novel aluminum-lithium alloy with different roll casting process parameters during twin-roll casting In: *Materials Characterization* Vol. 161, pp. 110145.

[15] KIHOULOU, B., KRALIK, R., BAJTOSOVA, L., GRYDIN, O., STOLBCHENKO, M., SCHAPER, M., CIESLAR, M. (2024) High-Temperature Phase Transformations in Al-Li-Cu-Mg-Zr-Sc Alloy Studied via In Situ Electron Microscopy In: *Materials* Vol. 17, pp. 644.

[16] DUWEZ, P., WILLIENS, R. H., KLEMENT, W. (1960) Continuous series of Metastable Solid Solutions in Silver-Copper Alloys In: *Journal of Applied Physics* Vol. 31, pp. 1136-1137.

[17] DUTKIEWICZ, J., KABISCH, O., GILLE, W., SIMMICH, O., SCHOLZ, R., KROL, J. (2022) Structure Changes and Precipitation Kinetics in Melt Spun and Aged Al–Li–Cu Alloy In: *International Journal of Materials Research* Vol. 92, pp. 0229.

[18] KIM, D. H., CANTOR, B., LEE, H. I. (1988) Structure and decomposition behaviour of rapidly solidified AI-Cu-Li-Mg-Zr alloys In: *Journal of Materials Science* Vol. 23, pp. 1695-1708.

[19] QI, Y., ZHANG, H., NIE, X., HU, Z., ZHU, H., ZENG, X. (2020) A high strength Al–Li alloy produced by laser powder bed fusion: Densification, microstructure, and mechanical properties In: *Additive Manufacturing* Vol. 35, pp. 101346.

[20] PU, Q., JIA, Z., KONG, Y., ZHANG, Z., YANG, Q., FAN, X., ZHANG, H., LIN, L., LIU,Q. (2020) Microstructure and mechanical properties of 2195 alloys prepared by traditional casting and spray forming In: *Materials Science and Engineering: A* Vol. 784, pp. 139337.

[21] LY, P., WANG, R., PENG, C., CAI, Z. (2023) Microstructural evolution and mechanical properties of 2195 Al-Li alloy processed by rapid solidification and thermo-mechanical processing In: *Journal of Alloys and Compounds* Vol. 948, pp. 169794.

[22] GIANOGLIO, D., CITFCI, N., ARMSTRONG, S., UHLENWINKEL, V., BATTEZZATI, L. (2021) On the Cooling Rate-Microstructure Relationship in Molten Metal Gas Atomization In: *Mettalurgical and Materials Transactions: A Vol.* 52, pp. 3750-3758.

[23] YANG, X., ZHANG, L., SOBOLEV, S., DU, Y. (2017) Kinetic Phase Diagrams of Ternary Al-Cu-Li System during Rapid Solidification: A Phase-Field Study In: *Materials* Vol. 11, pp. 260.

[24] GUSAKOVA, O., SHEPELEVICH, V., ALEXANDROV, D. V., STARODUMOV, I. O. (2020) Formation of the microstructure of rapidly solidified hypoeutectic Al-Si alloy In: *The European Physical Journal Special Topics* Vol. 229, pp. 417-425.

[25] GUSAKOVA, O. (2023) Chemically partitionless crystallization in near-eutectic rapidly solidified Al–12, 6Si–0, 8Mg–0, 4Mn–0, 7Fe–0, 9Ni–1, 8Cu alloy In: *The European Physical Journal Special Topics* Vol. 232, pp. 1281-1291.

[26] GRYDIN, O., GARTHE, K-U., YUAN, X., BROER, J., KESSLER, O., KRALIK, R., CIESLAR, M., SCHAPER, M. (2023) Numerical and Experimental Investigation of Twin-Roll Casting of Aluminum–Lithium Strips In*: Light Metals*, pp. 1031-1037.

[27] ESKIN, D., DU, Q., RUVALCABA, D., KATGERMAN, L. (2005) Experimental study

of structure formation in binary Al–Cu alloys at different cooling rates In: *Materials Science and Engineering: A* Vol. 405, pp. 1-10.

[28] CLYNE, D. W., KURZ, W. (1981) Solute redistribution during solidification with rapid solid state diffusion In: *Metallurgical Transactions* Vol. 12, pp. 965-971.

[29] FLEMINGS, M. C. (1974) Solidification processing In: *Metallurgical Transactions* Vol. 5, pp. 2121-2134.

[30] HADADZADEH, A., WELLS, M. A. (2013) Thermal fluid mathematical modelling of twin roll casting (TRC) process for AZ31 magnesium alloy In: *International Journal of Cast Metals Research* Vol. 26, pp. 228-238.

[31] GRYDIN, O., STOLBCHENKO, M., SCHAPER, M., BELEJOVA, S., KRALIK, R., BAJTOSOVA, L., KRIVSKA, B., HAJEK, M., CIESLAR, M. (2020) New Twin-Roll Cast Al-Li Based Alloys for High-Strength Applications In: *Metals* Vol. 10, pp. 987.

[32] WILLIS, D. J., LAKE, J. S. (1987) Measurement of grain size using the circle intercept method In: *Scripta Metallurgica Materialia* Vol. 21, pp. 1733-1736.

[33] DE POTTEY, A., JIANG, L., DORIN, T., WOOD, T., LANGAN, T., SANDERS, P. (2023) Effect of Cooling Rate on W-Phase Formation in Al-Cu-Sc Alloys In: *Light Metals* pp. 1238-1246.

[34] CIESLAR, M., KRIVSKA, B., KRALIK, R., BAJTOSOVA, L., GRYDIN, O., STOLBCHENKO, M., SCHAPER, M. (2022) HOMOGENIZATION OF TWIN-ROLL CAST AL-LI-BASED ALLOY STUDIED BY IN-SITU ELECTRON MICROSCOPY In: *Proceedings 31st International Conference on Metallurgy and Materials*, Brno, Czechia, May 18-19.

[35] CZERWINSKI, F. (2020) Thermal Stability of Aluminum Alloys In: *Materials* Vol. 13, pp. 3441.

[36] VANDERSLUIS, E., RAVINDRAN, C. (2017) Comparison of Measurement Methods for Secondary Dendrite Arm Spacing In: *Metallography, Microstructure and* Analysis Vol. 6, pp. 89-94.

[37] YANG, Q., SHI, W., WANG, M., JIA, L., WANG, W., ZHANG, H. (2023) Influence of cooling rate on the microstructure and mechanical properties of Al-Cu-Li-Mg-Zn alloy In: *Journal of Materials Research and Technology* Vol. 25, pp. 3151-3166.

[38] TOMKEIEFF, S. I. (1945) Linear Intercepts, Areas and Volumes In: *Nature* Vol. 24, pp. 155.

[39] KRALIK, R., BAJTOSOVA, L., KIHOULOU, B., PREISLER, D., CIESLAR, M. (2024) High-Temperature Phase Transformations in Al-Li-Cu-Mg-Zr-Sc Alloy Studied via In Situ Electron Microscopy In: *Crystals* Vol. 14, pp. 136.

[40] DANG, J., HUANG, Y., CHENG, J. (2009) Effect of Sc and Zr on microstructures and mechanical properties of as-cast Al-Mg-Si-Mn alloys In: *Transactions of the Nonferrous Metals Society of China* Vol. 19, pp. 540-544.

[41] QIN, J., TAN, P., QUAN, X., LIU, Z., YI, D., WANG, B. (2022) The effect of sc addition on microstructure and mechanical properties of as-cast Zr-containing Al-Cu alloys In: *Journal of Alloys and Compounds* Vol. 909, pp. 164686.

[42] XU, C., XIAO, W., ZHENG, R., HANADA, S., YAMAGATA, H., MA, C. (2015) The synergic effects of Sc and Zr on the microstructure and mechanical properties of Al–Si–Mg alloy In: *Materials and Design* Vol. 88, pp. 485-492.

[43] PRACH, O., TRUDONOSHYN, O., RANDELZHOFER, P., KORNER, C., DURST, K. (2020) Multi-alloying effect of Sc, Zr, Cr on the Al-Mg-Si-Mn high-pressure die casting alloys In: *Materials Characterization* Vol. 168, pp. 110537.

[44] GRYDIN, O., NEUSER, M., SCHAPER, M. (2023) Influence of Shell Material on the Microstructure and Mechanical Properties of Twin-Roll Cast Al-Si-Mg Alloy In: *Proceedings of the 14th International Conference on the Technology of Plasticity - Current Trends in the Technology of Plasticity Mandelieu* – La Napoule, France, September 24-29.

[45] PEET, M. J., HASAN, H. S., BHADESHIA, H. K. D. H. (2011) Prediction of thermal conductivity of steel In: *Internatiounal Journal of Heat and Mass Transfer* Vol. 54, pp. 2602-2608.

[46] GUO, S., LIU, Y. (2012) Estimation of critical cooling rates for formation of amorphous alloys from critical size In: *Journal of Non-crystalline Solids* Vol. 358, pp. 2753-2758.

[47] VICTORIA-HERNANDEZ, J., KURZ, G., BOHLEN, J., YI, S., LETZIG, D. (2021) Influence of Twin-Roll Casting Speed on Microstructural Homogeneity, Centerline Segregation, and Surface Quality of Three Different Mg Alloys In: *Developments in the*

Production of Magnesium Alloy Flat Products Vol. 73, pp. 76-81.

[48] ROYSET, J., RYUM, N. (2005) Scandium in Aluminum Alloys In: *International Materials Reviews* Vol. 50, pp. 19-44.

[49] LEI, Z., WEN, S., HUANG, H., WEI, W., NIE, Z. (2023) Grain Refinement of Aluminum and Aluminum Alloys by Sc and Zr In: *Metals* Vol. 13, pp. 751.

[50] WANG, L. (2018) Influence of Homogenization on Microstructural Response and Mechanical Property of Al-Cu-Mn Alloy In: *Materials* Vol. 11, pp. 914.

[51] STEFANESCU, D. M., RUXANDA, R. (2004) *ASM Handbook vol. 9 – Metallography and Microstructures*, pp. 107-115. ASM International, Detroit, MI, USA.

[52] SARREAL, J. A., ABBASCHIAN, G. J. (1986) The Effect of Solidification Rate on Microsegregation In: *Metallurgical Transactions: A* Vol. 17, pp. 2064-2073.